ADVANCED FUNCTIONAL MATERIALS
www.afm-journal.de

Understanding the Role of Hydrogen and Oxygen in Electronic Phase Changes of Nickelates

Laura Guasco, Rebecca Pons,* David Cortie, Lars J. Bannenberg, Peter Wochner, Eberhard Goering, Peter Nagel, Stefan Schuppler, Shohei Hayashida, Rotraut Merkle, Bernhard Keimer, Thomas Keller, and Eva Benckiser**

Many electronic and electrochemical devices rely on the exchange of light elements such as hydrogen and oxygen with the environment. Understanding and tailoring the device functionality requires accurate information about the concentration and chemical bonding of such species inside a solid, which is particularly difficult if several species are exchanged. In $LaNiO_3$ thin films in situ transport experiments reveal a re-entrant metal–insulator transition upon hydrogen exposure. The origin of this unusual behavior can be understood by combining information about the stoichiometry and chemical bonding of hydrogen and oxygen as determined by neutron reflectometry and x-ray absorption spectroscopy, respectively. In addition to the metallic parent phase, an insulating phase with composition $LaNiO_{2.65}$ and a re-entrant metallic phase with composition $LaNiO_{2.15}(OH)_{0.5}$ are identified. They can be inter-converted by redox reactions in different external environments. The methodology employed offers new insights into the mechanisms underlying the influence of hydrogen in functional devices.

1. Introduction

Reversible hydrogen doping offers particularly interesting possibilities for tuning the electronic properties of functional materials. When incorporated into a host matrix, hydrogen can induce reversible metal–insulator transitions[1–3] or selectively control superconductivity[4–6] and magnetic transitions,[7–10] paving the way for a new generation of hydrogen-based devices.[11,12] However, the development of new applications requires an in-depth understanding of the interaction between hydrogen and its host, including the precise quantification of the hydrogen content absorbed, and released. In particular, hydrogen can be incorporated in transition-metal oxides in different forms: as an interstitial proton H^+, bound as an H^- anion or as an OH^- ligand, or even as full water molecule. These different forms lead to significantly different valence states of the transition metals and influence the physical properties of the material. Especially in the case of thin films with large surfaces, the hydrogen uptake can change the properties over the entire film thickness.

An interesting material system is the rare-earth nickelates $RNiO_3$ with R = La-Lu, in which changes in resistivity have been observed when hydrogen is incorporated.[1,2,13,14] Even though hydrogen is commonly considered the only responsible for electronic modifications, the possible formation of oxygen vacancies is highly relevant as was found for $LaNiO_3$ (LNO) in the context of electro-catalysis for the oxygen evolution reaction.[15] In addition to electronic doping by hydrogen or oxygen vacancies, a change in the crystal structure due to the reaction with hydrogen can also result in a change in the sample properties.[16] Since nickelates are very sensitive to hydrogen, stable in harsh environments, compatible with conductive aqueous media,[17] and their resistance change being reversible and

L. Guasco, R. Pons, E. Goering, S. Hayashida, R. Merkle, B. Keimer, T. Keller, E. Benckiser
Max Planck Institute for Solid State Research
Heisenbergstraße 1, 70569 Stuttgart, Germany
E-mail: L.Guasco@fkf.mpg.de; R.Pons@fkf.mpg.de; E.Benckiser@fkf.mpg.de

The ORCID identification number(s) for the author(s) of this article can be found under https://doi.org/10.1002/adfm.202419253

DOI: 10.1002/adfm.202419253

L. Guasco, T. Keller
Max Planck Society Outstation at the Heinz Maier-Leibnitz Zentrum (MLZ)
85748 Garching, Germany

D. Cortie
Australian Nuclear Science and Technology Organisation (ANSTO)
New Illawarra Road, Lucas Heights, NSW 2234, Australia

L. J. Bannenberg, P. Wochner
Delft University of Technology
Mekelweg 15, Delft 2629 JB, Netherlands

P. Nagel, S. Schuppler
Institute for Quantum Materials and Technologies (IQMT) and Karlsruhe Nano and Micro Facility (KNMFi)
Karlsruhe Institute of Technology (KIT)
76021 Karlsruhe, Germany

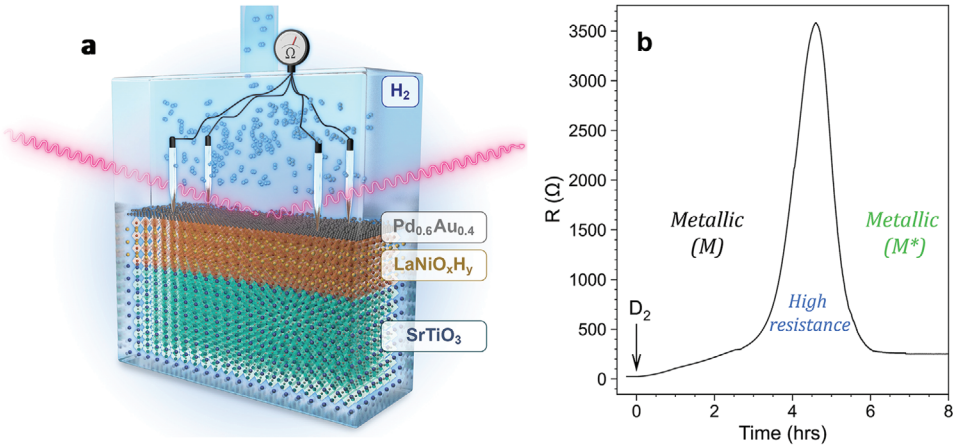

Figure 1. Electrical transport and simultaneous x-ray (neutron) scattering. a) Schematic of the experimental setup for in situ scattering and resistance measurements. The samples are placed in an atmosphere-controlled chamber connected to a vacuum pump and gas mixtures; b) In situ electrical transport under Ar/D_2 atmosphere at room temperature for 10 nm LNO film.

controllable through an electric field[18–20] they have been proposed as promising candidates for a range of applications: electric field sensors in salt water,[17] biosensing,[21] electrolyte for solid oxide fuel cells,[22] memory device,[20] microelectromechanical system actuators[23] and neuromorphic computing.[19,24–26] Further interest arises in connection with the recently discovered superconducting infinite-layer nickelates with composition $(R, A)NiO_2$ (A = alkaline-earth ion). These are usually synthesized by topotactic oxygen reduction through a reaction with CaH_2, which can also lead to hydrogenation, as has been shown for $NdNiO_3$,[27] and as well in superconducting films.[5] While the first experimental and theoretical studies pointed to a possible role of hydrogen in realizing superconductivity,[5,28,29] successive studies have ruled it out.[30–33] Interestingly, an unusual tendency for hydrogen intercalation was found for LNO, while it was assessed unfavorable in several other nickelate systems considered.[30] This lively debate demonstrates the urgency of addressing hydrogen and simultaneously oxygen stoichiometry in thin films reduced in different conditions.

In this work, we present an in-depth study of epitaxially grown LNO thin films, which shows a multi-step electronic and structural transformation when exposed to hydrogen gas at room temperature (RT). The hydrogenation of LNO, which is metallic in its pristine form, first induces a high resistance behavior followed by a second transition to another metallic phase. In situ, neutron reflectometry shows that these transitions are accompanied by considerable hydrogen incorporation with simultaneous oxygen loss. The unusual H and O stoichiometry in the hydrogenated LNO layer reduces the Ni valence significantly, as shown by x-ray absorption spectroscopy, accounting for the observed electronic transformation of the sample.

2. Results

To measure the changes in the film while exposed to the hydrogen atmosphere, we used a custom-built sample chamber, which is shown schematically in **Figure 1a** (see Experimental Section section for details). Electrical transport measured during the exposure at RT showed a steep increase of the resistance followed by a similarly steep decrease, until reaching an equilibrium state over a time-scale of a few hours with final resistance in the same order of magnitude of the initial values (Figure 1b). The system showed stable properties as long as it stayed in a hydrogen-rich atmosphere, however, we observed an immediate increase of the resistance when the sample surface was exposed to helium, vacuum or air (Figure S1, Supporting Information). It was possible to restore the pristine state of the samples through annealing in air at ambient pressure and 500°C for 1 h, while annealing in vacuum was not sufficient to reverse the reaction (Figure S2a,b, Supporting Information).

To investigate the incorporation of hydrogen in the different phases observed at room temperature, we performed x-ray reflectometry (XR) and neutron reflectometry (NR) experiments.

Figure 2a shows the experimental NR curves together with the model fits measured on the same sample successively annealed in air and then exposed to hydrogen or deuterium gas for over 12 h. The fitting parameters are summarized in **Table 1**. We find striking variations in both the thickness and scattering length density (SLD) of the LNO layer. The thickness increases ≈18% after exposure to hydrogen or deuterium, and is restored to its original value after the annealing procedure. This large increase in volume of the perovskite film can be ascribed to both oxygen loss and hydration, as we will discuss below. The SLD on the other hand is reduced to a different degree after H_2 and D_2 exposure, indicating incorporation of hydrogen atoms in the film.

By using the isotope contrast of hydrogen and deuterium, the amount of hydrogen absorbed by the film can be accurately determined assuming for both isotopes that the same equilibrium phase is reached at the end of the reaction: $LaNiO_{3-\delta}H_x$. Then, by simple algebraic substitution, it follows that:

$$x = \frac{\Delta SLD}{\gamma(b_D - b_H)} \quad (1)$$

where x is the hydrogen concentration, ΔSLD is the difference between the SLD of the LNO layer exposed to deuterium and hydrogen, γ is the atomic density of the LNO layer and b_D and b_H are the scattering length of deuterium and hydrogen,

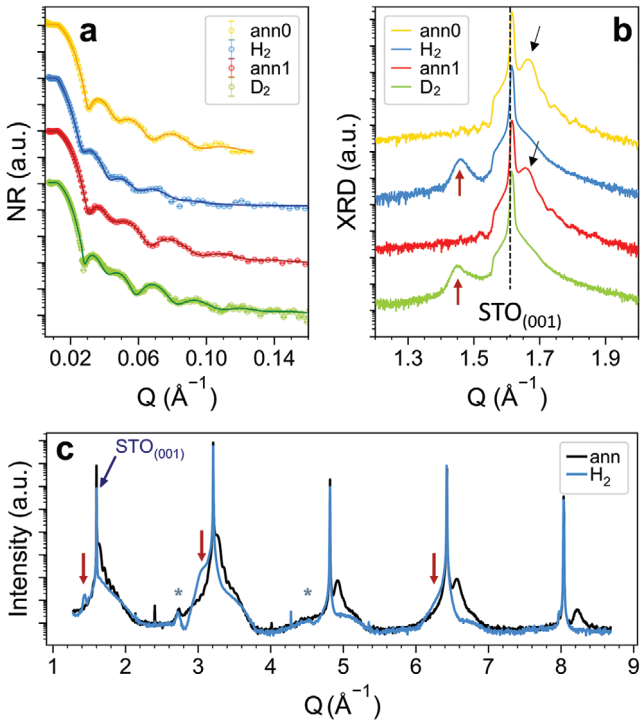

Figure 2. Structural characterization of the LNO film after sequential annealing and subsequent hydrogen and deuterium exposure by complementary neutron and x-ray experiments. Panel a): In situ neutron reflectometry; panel b): X-ray diffraction measured on the same sample after annealing (labeled ann0 and ann1) or gas exposure of the annealed sample (H_2 and D_2 labeled curves); panel c) XRD scan along 00L comparison between the state after annealing (ann) and the hydrogenated state (H_2). The red arrows highlight the new features after gas exposure and the gray stars indicate the peaks attributed to the PdAu capping layer.

respectively. Our results show absorption of 0.51 hydrogen atoms per formula unit, i.e. one hydrogen atom per two Ni atoms. Fixing this value for the H/D content and considering the layer expansion we still find a reduced SLD for the LNO layer, which can be explained by a change of the oxygen stoichiometry from 3 to 3 - δ. The calculation gives $\delta = 0.35$, which corresponds to a film stoichiometry of $LaNiO_{2.65}H_{0.51}$. Additional NR experiments performed on thinner samples with 10 nm LNO confirmed a comparable and reproducible amount of absorbed hydrogen and reduced oxygen content.

To exclude a possible influence of the capping layer and substrate in the observed electrical and structural transformation, we conducted additional transport and NR measurement on 5 nm thick $Pd_{0.6}Au_{0.4}$ layers deposited on $SrTiO_3$ (STO).

Table 1. Fitting parameters and their statistical uncertainty.

	d_{LNO} [Å]	d_{PdAu} [Å]	SLD_{LNO} [10^{-6}Å^{-2}]	SLD_{PdAu} [10^{-6}Å^{-2}]
ann0 (*M*)	196.6 ± 1.1	79.3 ± 0.7	5.94 ± 0.01	4.83 ± 0.06
H_2 (*M**)	235.5 ± 1.0	80.0 ± 0.6	**4.712** ± 0.006	3.54 ± 0.03
ann1 (*M*)	202.4 ± 0.5	82.6 ± 0.4	6.053 ± 0.008	4.35 ± 0.03
D_2 (*M**)	235.2 ± 0.4	85.6 ± 0.4	**5.509** ± 0.006	3.77 ± 0.02

The results, shown in Figure S3 (Supporting Information), exhibited no change before and after hydrogen exposure, which clearly ruled out the possibility that the observed resistivity and NR changes at RT are due to transformations of the catalyst layer.

Prior and immediately after each NR experiment, additional ex situ x-ray reflectivity (Figure S4, Supporting Information) and diffraction (Figure 2b) measurements were performed. The fitting of XR curves confirmed the thickness swelling and density decrease observed after gas exposure in NR (Table S1, Supporting Information) and in additional in situ XR results shown in the Figure S5 (Supporting Information). While XR and NR provide depth profiles of the electron or nucleus density, respectively, x-ray diffraction (XRD) provides information on the crystalline properties of the sample, i.e. about the atomic distances and the symmetry of the crystal. For the pristine and annealed sample we clearly observe a series of (00L) peaks attributed to the perovskite LNO phase, with a pseudo-cubic (pc) *c*-axis $c_{pc} = 3.824$ Å. This value is slightly larger than what is expected for $LaNiO_3$ on STO,[34] which can be explained by oxygen vacancy formation (studied in detail e.g. for $SmNiO_{3-\delta}$[35]). The annealed film's $(001)_{pc}$ reflections in Figure 2b are intense and superimposed by Laue thickness oscillations, indicating good coherence and epitaxial growth of the LNO layer and its recovery through annealing. After exposure to the reducing atmosphere the perovskite peaks disappear and new peaks appear at substantially lower *Q*, indicated by red arrows. Assuming a simple out of plane lattice expansion of the perovskite, this would correspond to a colossal 13% increase in the *c* parameter, similar to that reported in ref. [36]. The lattice expansion alone is not sufficient to explain the total thickness increase observed by NR and XR, suggesting the formation of macroscopic defects or cracks in the layer upon hydrogenation. The formation of disorder is also seen in the in situ, wide-range out-of-plane XRD scan (Figure 2c) and reciprocal space maps (Figure S9a,b, Supporting Information), which shows all the perovskite film peaks diminish and broaden after hydrogenation. Only the (001) reflection exhibits a distinct sharper feature, suggesting that a different crystal structure is formed, the detailed properties of which remain to be determined in a future study.

All results shown in Figure 2 and Table 1 discussed so far present an equilibrium state either before introducing hydrogen or after the sample was exposed to the atmosphere for several hours and no changes were detectable anymore.

To gain insight into the kinetics and stability of the hydrogenation process, we followed the changes in the sample with continuous measurement of short NR scans (**Figure 3a**). Using an automated routine, a simple model was fitted to each of the reflectivity curves to extract the most relevant parameters, the thickness and SLD of the LNO film, as a function of time after the introduction of the gas atmosphere. Figure 3b shows the results for the nickelate SLD. The empty circles are extracted from the short scans with momentum transfer *Q* up to 0.045 Å^{-1} and thus have larger errors, while the diamonds correspond to the extensive scans from Figure 2a/Table 1. The previously made assumption that the film would reach a state of equilibrium is confirmed by the stability of the fitting parameters, which are reached after ≈500 min and agree well with the values extracted from the

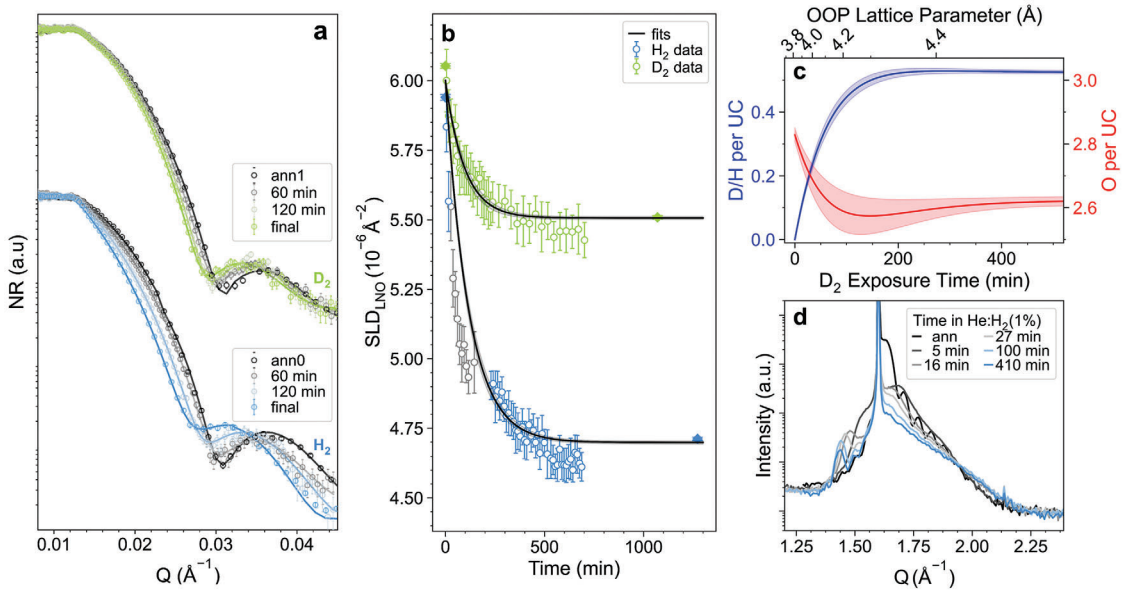

Figure 3. Changes in the LNO film over time during H_2 and D_2 loading. a) In situ continuous NR scans measured during the H_2 and D_2 loading. Solid lines show the fit to the model curve. For clarity only selected scans are shown (more details on the fast changes at the beginning of the gas exposure in Figure S7a, Supporting Information); b) SLD of the LNO film extracted by the automatic fitting routine from fast short reflectivity scans taken during loading "(gray points indicate scans with unstable chamber pressure that were therefore excluded from the fit, for more details see Figure S6, Supporting Information)"; c) hydrogen and oxygen content per unit cell (UC) versus time and out-of-plane (OOP) lattice expansion extracted from NR fits of the thickness and SLD; d) (001) peak evolution during hydrogenation from in situ XRD.

long scan. The changes are faster in the beginning and their time dependence, tracked by SLD in Figure 3b, resembles an exponential decay.

Our observations over several measurements on different samples suggest that the hydrogenation speed is hydrogen partial pressure and cycle dependent (Figure S9, Supporting Information). For this reason, we have used the hydrogenation-dependent layer thickness variation as a measure of the status of the reaction process. Using the same equations as above, the hydrogen and oxygen content can then be calculated over time (Figure 3c), with the time scale of the hydrogen data set rescaled to match the one of the deuterium run. The calculated initial oxygen content is not three as for a perfectly stoichiometric perovskite, indicating that the sample is not fully reoxidized after annealing in air, which is consistent with the slightly larger c_{pc} extracted from the XRD data. This is likely due to the presence of the catalytic layer, which enables partial oxygen vacancy formation already at ambient conditions. However, after application of the hydrogen atmosphere, the sample clearly loses oxygen at the same time as it takes up hydrogen. This suggests a dual-ion transformation, as has been observed in other perovskite systems.[7,41]

To follow the structural changes during the process, additional synchrotron XRD measurements were carried out under in situ exposure with He:H_2 gas (Figure 3d). Similar to the process monitored with neutrons, the changes occur fast in the beginning and then slow down. The shorter time scale compared with the neutron measurements can be attributed to the higher H_2 partial pressure. The observed new $(001)_{pc}$ peak developed during hydrogenation and gradually separated from the original perovskite peak, with the intensity of the latter decreasing and its width increasing. Hydrogenation expands and reshapes the lattice, creating disorder and presumably changing the overall structure. The hydrogenated phase (M*) is metastable. Once hydrogen is removed from the atmosphere, e.g. replaced by pure He, in situ XRD shows the peak immediately shifting back toward lower c_{pc} (Figure S9, Supporting Information).

With the composition of $LaNiO_{2.65}H_{0.51}$ precisely determined from neutron reflectometry, the question arises as to the form in which the hydrogen is incorporated, i.e. as H^+ or H^- ion. To gain insight into this, we have performed soft x-ray absorption spectroscopy (XAS) measurements on the hydrogen-loaded film and confirmed the metastability on a sample left one day in air (labeled S). The measurements at the Ni-*L* edge and their linear polarization dependence provide insight into the Ni valence state and the crystal field, respectively (**Figure 4a**), and the spectra at the O-*K* edge reflect the site- and symmetry-projected hybridization of cations forming covalent bonds with oxygen (Figure 4b).

Soft XAS data for the $Ni(OH)_2$-NiOOH redox system, analyzed in the context of water electrolysis or cathode materials, provide a good refs. [39, 42, 43]. The comparison suggests that an oxyhydroxide $LaNiO_{2.15}(OH)_{0.5}$ with $Ni^{1.8+} \sim$ Ni(II) is formed during hydrogen loading. The Ni-*L* edge XAS compared to $LaNiO_3$, NiO and $LaNiO_2$ as well as the O-*K* pre-peak at 532 eV are indicative of Ni(II), which is also consistent with hydroxide formation. We conclude that hydrogen is incorporated as protons in the nickelate film. The near absence of linear dichroism in the Ni-*L* spectra indicates that the OH ligands randomly replace the O^{2-} ions in apical and basal positions of the NiO_6 octahedra. However, a previous study of related β-NiOOH has shown that hydrogenation does not occur at opposite oxygen atoms in the octahedron.[44]

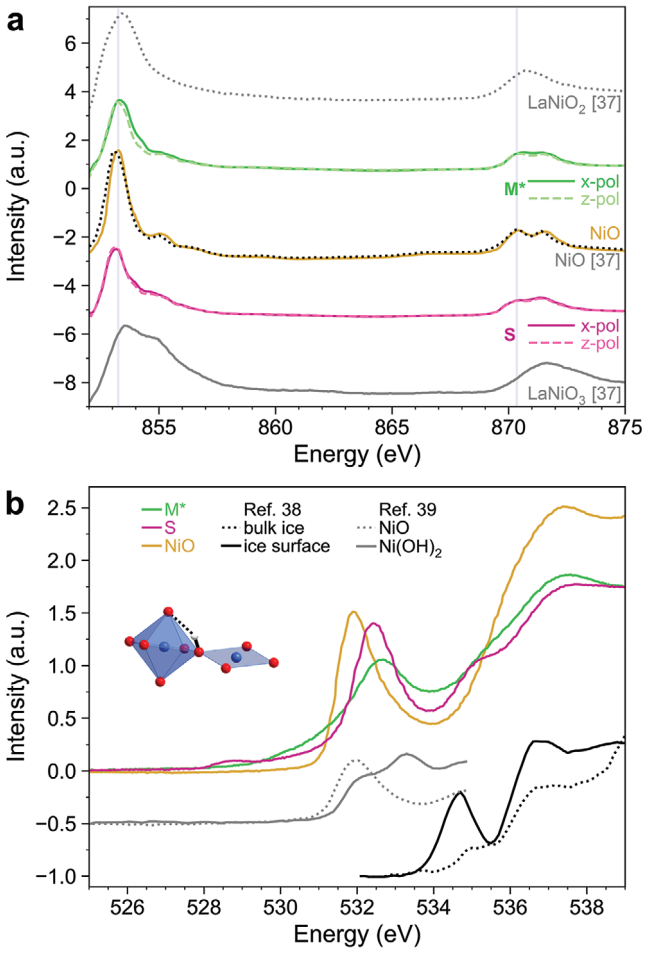

Figure 4. Near-edge x-ray absorption fine structure at **a** the nickel-$L_{3,2}$ and **b** oxygen-*K* edge. Both panels compare the spectra recorded on the LNO film immediately after hydrogen exposure (M*) and after leaving the film in air for one day (S). All spectra were normalized at energies well above the edge. The Ni-*L* spectra were measured with linearly polarized x-rays, with the electric field vector in the plane (*x*-pol.) and out of the plane of the film (*z*-pol.). For easier comparison spectra extracted from refs. [37,38] and [39] have been plotted as well with some offset for visibility. The data of ref. [37] are also shifted in energy to match the La-M_4 line's position. The La-M_4 line in each data set, which is partially overlapping with the Ni-L_3 line, was fitted with a Lorentzian and subtracted. The inset in panel **b** illustrates the incorporation of hydrogen as a hydroxide anion into the structure of $LaNiO_{2.5}$,[40] where the OH ligands form OH–O bridges along the octahedral edges.

When the hydrogen atmosphere is removed, i.e. M* → S, the oxyhydroxide decomposes with time:

$$4\,LaNiO_{2.15}(OH)_{0.5} + \frac{1}{2}O_2 \rightarrow 4\,LaNiO_{2.65} + H_2O \quad (2)$$

The accompanying formal Ni valence change from $Ni^{1.8+}$ to $Ni^{2.3+}$ could explain the changes in the fine structure of the L_3 edge at 855 eV and the altered ratio of the double-peak structure at the L_2 edge.[43] A further indication of this decomposition is the growth of the Ni(III)-O hybridized pre-peak at the O-*K* edge at 528 eV. The intensity between 534 and 537 eV is higher in M* (Figure 4 **b**), consistent with the peak present for $Ni(OH)_2$ and water molecules with one uncoordinated O-H group,[38,39] and decreases in phase S.

The temperature dependence of the resistance of the film at various stages of the reaction was investigated by cooling down to 3.5 K (**Figure 5a**). While the untreated sample shows the typical metallic behavior (M) of LNO, the final state (M*) shows a different metallic behavior, indicating a metal-to-metal transition ≈200 K followed by a slight increase below 15 K (Figure S10, Supporting Information), reminiscent of the upturn observed in undoped $NdNiO_2$ reduced with CaH_2.[45] After a few days in air, the layer (S) shows a semiconducting temperature dependence of resistance (red dashed line in Figure 5a), a clear change compared to the final state (M*), but no return to the pristine state (M). By annealing at 500 °C over several cycles we reproduced the metallic characteristic curve of the pristine state, with a slight increase of the residual resistivity ratio, indicating more defects in the system after each hydrogen exposure and air annealing (Figure S11, Supporting Information).

3. Discussion

A modification of the electronic properties of nickelates upon interacting with hydrogen has been observed in several experiments: i) Reduction with CaH_2, leading to the gradual removal of apical oxygen atoms from the perovskite to the infinite-layer phase, ii) hydrogen incorporation by catalyst-assisted H_2 gas exposure,[1,20] or iii) gating with ionic liquids (IL).[46] The methods utilized to characterize the obtained new phases were various, for example, secondary-ion mass spectroscopy[5,36] or nuclear reaction analysis[16] were used to detect hydrogen in thin films. In addition to being ex situ, these techniques are either destructive to some degree or indirect, contrarily to the isotope-contrast NR measurement used by us. Photo-electron spectroscopy and XAS were measured to confirm an increased ratio of Ni^{2+} with respect to Ni^{3+} in hydrogenated samples,[1,47] similar to our observation. Correspondingly, XRD characterization found unit cell volume expansion in both CaH_2 reduced samples[48] (dry atmosphere) and, to a bigger degree, in wet environments such as IL-gated $NdNiO_3$.[36] The comparison with these works suggests that both oxygen reduction and hydration contribute to the giant swelling observed by us. The concomitant loss of oxygen was generally not considered or observed in catalyst-assisted hydrogenation or IL gating works, even though the phenomenon of simultaneous hydrogen inclusion and oxygen loss is known to occur for other transition-metal oxides.[7,41,49] Due to the high mobility of hydrogen and oxygen ions in oxides, it is essential to choose a set of characterization tools that allows for in situ, quantitative and non-destructive measurements, such as our in situ neutron reflectometry in combination with resistance measurements and XAS. Combining the information from all these diverse measurement methods, we can sketch a complete picture of the reaction cycle in Figure 5b.

When the pristine, metallic $LaNiO_3$ film with a catalytic layer (I) is exposed to a hydrogen atmosphere at RT, some of the hydrogen ions combine with oxygen to form water molecules, which are leaving the film, while another part remains in the LNO film in the form of OH anions (Phase II). The final phase that can be reached under these conditions is the metallic oxyhydroxide $LaNiO_{2.15}(OH)_{0.5}$ with a formal valence state of $Ni^{1.8+}$. However,

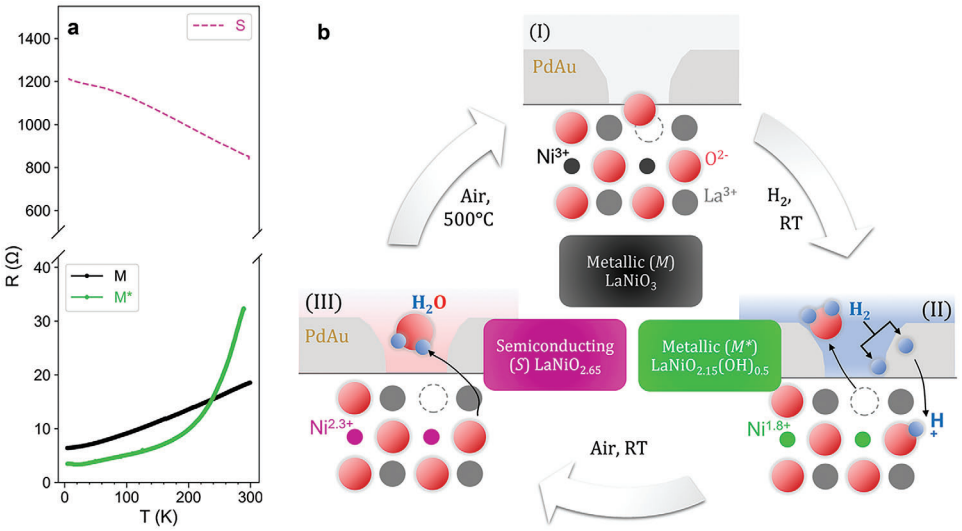

Figure 5. Electronic modifications of the LNO layer when exposed to reducing and oxidizing atmosphere. a) Electrical transport upon cooling at various reaction stages; b) schematics of redox reaction cycle between M (I), M* (II) and S (III) LNO layers upon exposure to hydrogen gas, air at RT and air at 500°C.

this phase is only metastable, because when the hydrogen atmosphere is replaced by air, the hydrogen start to migrate to the surface until they reach the catalyst and form water bonding the oxygen present in the air (III). At RT the oxygen stoichiometry does not change, forming the semiconducting $LaNiO_{2.65}$ with the Ni oxidation state increasing to $Ni^{2.3+}$. Finally, when heating the oxygen deficient $LaNiO_{2.65}$ in air at 500 °C the initial metallic $LaNiO_3$ phase can be recovered (I).

With the exception of ref. [50], previous studies[1,2,14,20] only observed the metal-to-insulator transition part of the reaction which is likely due to inhomogeneity, with patches of LNO at different stages of the reaction. In our case the sample was thin and the catalyst covered the entire surface ensuring homogeneous hydrogenation, while so far samples were prepared with Pt patterns, thus never generating a continuous path of hydrogen-rich LNO like ref. [50] achieved with connected grain boundaries. The final phase reached with patterned Pt is stable in air and poor in hydrogen, fitting what we labeled S phase.

Another process involving hydrogen and modifying the oxygen stoichiometry in nickelates is the reduction by CaH_2, but the chemical reaction is substantially different. Hydrogen released from the hydride seizes oxygen from the nickelate layer, and is then bonded to the Ca^{2+} ions, when in direct contact, to form $Ca(OH)_2$ hydroxide. Reduced by CaH_2 the final state of LNO is metallic too, but without further experiments it remains unclear whether the similarly low Ni valence is achieved by oxygen loss or hydrogen doping, or even a combination of the two.

4. Conclusion

In conclusion, we observed a cycle between three phase transitions at room temperature by exposing an epitaxial $LaNiO_3$ thin film capped with a catalytic Pd-Au layer to hydrogen gas. In situ, non-destructive neutron reflectometry revealed a concomitant hydrogen incorporation and oxygen loss at the origin of the structural and electronic modifications of the nickelate layer. XAS spectra indicated an average reduced Ni valence, and presence of hydroxyl groups inside the thin film. Our results for the nickelates explain the observed switching behavior exploited in multiple device designs and represents an alternative method to study the mobility of oxygen in the lattice under reaction with hydrogen, which is critical for its electrocatalytic activity. This study shows the importance of using the appropriate combination of techniques to unveil the real stoichiometry and nature of bonds between atoms in systems and processes that involve hydrogen and oxygen. Going beyond nickelates, this approach can be extended to other transition metal oxide electrocatalyst candidates or proton-based functional materials. The high mobility of light atoms at ambient conditions makes it essential to perform in situ studies to have a full picture of the reaction at work.

5. Experimental Section

Thin Film Growth: The investigated samples were grown by molecular beam epitaxy (MBE) on 10 × 10 mm^2 (100)-oriented STO substrates. The 10–20 nm thick LNO films were grown by sequentially opening the La and Ni effusion cells with the substrate temperature at ≈600 °C in a 2.4×10^{-5} mbar ozone atmosphere and cooled down keeping the ozone pressure. To add the catalytic capping layer the sample remained in the chamber, the ozone was pumped out and with the sample at room temperature the Pd and Au effusion cells were opened simultaneously until ≈3–5 nm were deposited. The composition $Pd_{0.6}Au_{0.4}$ was chosen in order to have a good hydrogenation kinetics and limited expansion which could cause strain. Following a study from L. Bannenberg et al.[51] Pd has a fast response time and alloying it with 40% Au even enhances this while also suppressing the transition to the $PdH_x\beta$-phase at higher hydration reducing the volumetric expansion thus improving cyclability. Before growth the fluxes were calibrated in vacuum with a quartz crystal microbalance (QCM) matching the Pd flux to 1.5-times the Au flux. During the growth of the nickelate the Ni shutter opening time was adjusted according to the reflection high-energy electron diffraction (RHEED) feedback. For more details on the MBE system see ref. [52].

Hydrogen Exposure: The LNO films were exposed to hydrogen atmosphere at room temperature in a custom-made air-tight cell throughout

this study. The chamber included inlets for connection to a vacuum pump and gas bottle. Two types of mixtures were typically used: $A_{1-x\%}/H_{2x\%}$ or $A_{1-x\%}/D_{2x\%}$, with A being an inert gas such as Ar or He and x the concentration of hydrogen gas between 2% to 4%. The use of mixtures was preferred to pure gases due to safety reasons. Argon mixture was initially chosen as the more commonly available, but due to its high absorption of x-rays it was replaced by He for all synchrotron XRD measurements. Typical gas pressure used during the transport, XR and NR measurements were of 100–200 mbar static atmosphere, while a pressure of 1 bar was used for the in situ synchrotron XRD measurement. Annealing in the air to restore the sample after hydrogen exposure was performed at ambient pressure and 500°C for 1 h. Furthermore, one should note, that increased roughness of the capping layer was observed after each loading and annealing step so samples that were cycled more than about four times received a new capping layer in the MBE which increased the reaction speed again.

Electrical Transport: A four-point contact probe compatible with scattering experiments was realized with four spring-loaded pins pressed on the surface in the sample's corners. The current of 1 µA was applied along two adjacent contact and the voltage arising was measured along the two opposite ones. A Lakeshore M81 lock-in amplifier was used to reduce the noise and improve the signal. Due to the µm size of the pins tips the scattering path of x-ray and neutrons remained unaffected.

Neutron Reflectometry: Reflectometry is a technique that allows to quantify the depth-dependent structural properties of thin films in terms of the scattering length density (SLD), which is a quantity that accounts for the scattering potential of different atoms weighted by their atomic density.[53] X-ray and neutrons are complementary probes as their scattering potential on the same materials can be widely different. While x-rays interact with the electrons, neutrons are scattered by the nuclei.[54] Light elements, such as hydrogen, are practically invisible to x-rays due to the low electron density. However, the negative scattering length of the hydrogen nucleus provides a strong contrast in the scattering of neutrons. In addition, the contrast with deuterium was used, which has almost the same chemical properties but a positive neutron scattering length. Details of the calculation for the hydrogen and oxygen stoichiometry are found in Note S1 (Supporting Information).

Time-of-flight neutron reflectometry (NR) was performed at the SPATZ reflectometer at ANSTO.[55] The wavelength resolution $\Delta\lambda/\lambda$ was set to 5% and the slits were chosen to have an angular resolution $\Delta\theta/\theta$ of 5% too. Reflected neutrons were collected in a 2D position sensitive ^{3}He detector. Samples were placed in a specialized DEC-1 chamber for controlled temperature and gas exposure. For each sample long NR curves were acquired before and after hydrogenation covering a q_z range from 0.007 to 0.173 Å^{-1} with three incident angles of 0.6°, 2.2°, and 4.0°. Prior to hydrogen loading, the chamber was first evacuated and then 150 mbar of either H_2(3.5%)/Ar(96.5%) or D_2(4%)/Ar(96%) mixture were inserted in the chamber. During hydrogen exposure consecutive low-Q range scans up to 0.044 Å^{-1} at incident angle 0.6° of 60 s each were recorded continuously until no further changes in NR were observed. The data was then subsequently grouped in batches of 10 min to improve statistics and reduce the error bars for the batch fitting. All data were reduced and normalized utilizing in-house scripts.

The capping layer experiments and preliminary LNO trials were also performed at the ROG neutron reflectometer of the TU Delft reactor,[56] with in situ transport setup to measure in situ the resistance changes upon hydrogen exposure. The incident angle was set at 0.43° and the wavelength resolution was set to 6%. The gas exposure procedure was performed in a custom cell with simultaneous transport measurements as described above.

The fitting of all the reflectivity curves was performed with Refnx[57] and GenX.[58] Statistical uncertainty analysis was made via the "Bumps" library of GenX (open source software) to estimate the fitting parameters cross-correlation and uncertainties for the results on the initial and final states. In the automated fitting routine of the fast short NR scans, the error bars for the parameters were determined through 5% increase in the optimal figure of merit. These errors are used as weights for the subsequential exponential fit, in which the errors were determined by the python routine curve_fit (library scipy.optimize; open source). The displayed error bands in Figure 3c are calculated from error propagation with the variance formula from these fit errors.

X-Ray Measurements: The samples were preliminary characterized via XR at NREX,[59] and via XRD at the rotating anode facilities of the MPI-FKF in Stuttgart. Additional XR and XRD were performed with the rotating anode SmartLab at ANSTO.

In situ XR measurements were performed at NREX, at the FRM II, with the in-house built cell for hydrogen loading.

Synchrotron high-resolution diffraction (in main text Figure 2c and Figure 3d) was performed at the KIT Light Source at the Karlsruhe Research Accelerator (KARA), at the MPI-FKF beamline. The wavelength of 1.24 Å was used. Reciprocal space maps were reconstructed from the 2D Eiger detector images, through the software Binoculars.[60] During the measurement the atmosphere around the sample was either pure He gas, a H_2(1%)/He(99%) mixture or air at always ≈1 bar pressure.

XAS measurements were performed in total electron yield mode (TEY) at IQMT's soft x-ray beamline WERA at KARA. To ensure consistent energy calibration between our measurements, the NiO absorption spectra in the I_0 signal at the KIT Light Source were compared and the data were shifted by a small energy offset where necessary. When comparing with the literature data of ref. [37], it was assumed that the La-*M* edge remains unchanged and shifted all spectra of ref. [37] by 0.5 eV to higher energies. Note that this shift also brings the NiO reference measurement in agreement with the spectrum which was measured on a NiO powder (yellow curve in Figure 4a).

After using it for alignment each La line was fitted with a Lorentzian and subtracted. The O-*K* spectra from refs. [38] and [39] were plotted as published since the NiO pre-peak in ref. [39] is consistent with ours and there is no common reference line for the data from ref. [38].

Supporting Information

Supporting Information is available from the Wiley Online Library or from the author.

Acknowledgements

The KIT Institute for Beam Physics and Technology (IBPT) is acknowledged for the operation of the storage ring Karlsruhe Research Accelerator (KARA), and for provision of beamtime at the KIT Light Source. The neutron results shown here were obtained at the Spatz instrument operated at the Australian Nuclear Science and Technology Organization and at the ROG neutron reflectometer at the TU Delft Reactor Institute. The authors sincerely thank Nico Bonmassar for the deposition of catalytic layers, Michel Thijs for technical support and measurements at the TU Delft Reactor and Chris Baldwin and Anton Le Brun for the technical support and assistance during the measurements at ANSTO. The authors would like to acknowledge the MLZ Physics Lab, and in particular Bastian Veltel and Markos Skoulatos, for the use of the muffle furnace used to anneal the samples in air and for complementary XRD measurements. The authors would like to thank Reiner Mueller (FRM II / TUM) for the creation of the graphic model for Figure 1a. The authors would like to thank Luca Camuti for the internal review of our manuscript and Ke Zou for fruitful discussions.

Open access funding enabled and organized by Projekt DEAL.

Conflict of Interest

The authors declare no conflict of interest.

Author Contributions

L.G. and R.P. contributed equally to this work. L.G., R.P., E.B., and B.K. conceived the study. R.P. prepared the samples, L.G. performed transport

measurements. L.G. and R.P. were in charge of the NR experiments, with substantial help from T.K., L.B., and S.H. at the ROG reflectometer, and from D.C. and T.K. at Spatz. E.G., P.W., R.P., and L.G. performed the synchrotron experiments with technical support from P.N., S.S. L.G. and R.P. analyzed neutron and synchrotron data. All authors discussed the experimental results. L.G., R.P., and E.B. wrote the manuscript with contributions from all authors.

Data Availability Statement

The data that support the plots within this paper are available at the Open Research Data Repository of the Max Planck Society [L. Guasco, R. Pons et al. Source data for 'Understanding the Role of Hydrogen and Oxygen in Electronic Phase Changes of Nickelates'. Edmond – Open Research Data Repository for the Max Planck Society https://doi.org/10.17617/3.HSPKSY (2024).]. The data that support the findings shown in the Supplementary Information are available on request from the corresponding author.

Keywords

correlated oxides, hydrogen induced electronic transitions, hydrogen quantification, nickelates, re-entrant metallicity, reversible phase changes

Received: October 13, 2024
Revised: December 4, 2024
Published online:

[1] J. Shi, Y. Zhou, S. Ramanathan, *Nat. Commun.* **2014**, *5*, 4860.
[2] J. Chen, Y. Zhou, S. Middey, J. Jiang, N. Chen, L. Chen, X. Shi, M. Döbeli, J. Shi, J. Chakhalian, S. Ramanathan, *Appl. Phys. Lett.* **2015**, *107*, 3.
[3] C. Oh, S. Heo, H. M. Jang, J. Son, *Appl. Phys. Lett.* **2016**, *108*, 122106.
[4] X. Wei, H.-B. Li, Q. Zhang, D. Li, M. Qin, L. Xu, W. Hu, Q. Huan, L. Yu, J. Miao, J. Yuan, B. Zhu, A. Kusmartseva, F. V. Kusmartsev, A. V. Silhanek, T. Xiang, W. Yu, Y. Lin, L. Gu, P. Yu, Q. Chen, K. Jin, *Sci. Bull.* **2020**, *65*, 1607.
[5] X. Ding, C. C. Tam, X. Sui, Y. Zhao, M. Xu, J. Choi, H. Leng, J. Zhang, M. Wu, H. Xiao, X. Zu, M. Garcia-Fernandez, S. Agrestini, X. Wu, Q. Wang, P. Gao, S. Li, B. Huang, K.-J. Zhou, L. Qiao, *Nature* **2023**, *615*, 50.
[6] K. Takada, H. Sakurai, E. Takayama-Muromachi, F. Izumi, R. A. Dilanian, T. Sasaki, *Nature* **2003**, *422*, 53.
[7] N. Lu, P. Zhang, Q. Zhang, R. Qiao, Q. He, H.-B. Li, Y. Wang, J. Guo, D. Zhang, Z. Duan, Z. Li, M. Wang, S. Yang, M. Yan, E. Arenholz, S. Zhou, W. Yang, L. Gu, C.-W. Nan, J. Wu, Y. Tokura, P. Yu, *Nature* **2017**, *546*, 124.
[8] S. Shen, Z. Li, Z. Tian, W. Luo, S. Okamoto, P. Yu, *Phys. Rev. X* **2021**, *11*, 021018.
[9] J. Lee, Y. Ha, S. Lee, *Adv. Mater.* **2021**, *33*, 2007606.
[10] Z. Li, Y. Lyu, Z. Ran, Y. Wang, Y. Zhang, N. Lu, M. Wang, M. Sassi, T. D. Ha, A. T. N'Diaye, P. Shafer, C. Pearce, K. Rosso, E. Arenholz, J.-Y. Juang, Q. He, Y.-H. Chu, W. Luo, P. Yu, *Adv. Funct. Mater.* **2023**, *33*, 2212298.
[11] J. de Rojas, A. Quintana, G. Rius, C. Stefani, N. Domingo, J. L. Costa-Krämer, E. Menéndez, J. Sort, *Appl. Phys. Lett.* **2022**, *120*, 070501.
[12] Y. Wu, D. Li, C. Wu, H. Y. Hwang, Y. Cui, *Nat. Rev. Mater.* **2023**, *8*, 41.
[13] Y. Bian, H. Li, F. Yan, H. Li, J. Wang, H. Zhang, Y. Jiang, N. Chen, J. Chen, *Appl. Phys. Lett.* **2022**, *120*, 9.
[14] I. Matsuzawa, T. Ozawa, Y. Nishiya, U. Sidik, A. N. Hattori, H. Tanaka, K. Fukutani, *Phys. Rev. Mater.* **2023**, *7*, 8.
[15] E. M. Kiens, M.-J. Choi, L. Wei, Q. Lu, L. Wang, C. Baeumer, *Chem. Commun.* **2023**, *59*, 4562.
[16] J. Chen, W. Mao, B. Ge, J. Wang, X. Ke, V. Wang, Y. Wang, M. Döbeli, W. Geng, H. Matsuzaki, J. Shi, Y. Jiang, *Nat. Commun.* **2019**, *10*, 694.
[17] Z. Zhang, D. Schwanz, B. Narayanan, M. Kotiuga, J. A. Dura, M. Cherukara, H. Zhou, J. W. Freeland, J. Li, R. Sutarto, F. He, C. Wu, J. Zhu, Y. Sun, K. Ramadoss, S. S. Nonnenmann, N. Yu, R. Comin, K. M. Rabe, S. K. R. S. Sankaranarayanan, S. Ramanathan, *Nature* **2018**, *553*, 68.
[18] U. Sidik, A. N. Hattori, R. Rakshit, S. Ramanathan, H. Tanaka, *ACS Appl. Mater. Interfaces* **2020**, *12*, 54955.
[19] S. Gamage, S. Manna, M. Zajac, S. Hancock, Q. Wang, S. Singh, M. Ghafariasl, K. Yao, T. E. Tiwald, T. J. Park, D. P. Landau, H. Wen, S. K. R. S. Sankaranarayanan, P. Darancet, S. Ramanathan, Y. Abate, *Acs Nano* **2024**, *18*, 2105.
[20] Q. Wang, H. Zhou, S. Ramanathan, *ACS Appl. Electron. Mater.* **2022**, *4*, 2463.
[21] H.-T. Zhang, F. Zuo, F. Li, H. Chan, Q. Wu, Z. Zhang, B. Narayanan, K. Ramadoss, I. Chakraborty, G. Saha, G. Kamath, K. Roy, H. Zhou, A. A. Chubykin, S. K. R. S. Sankaranarayanan, J. H. Choi, S. Ramanathan, *Nat. Commun.* **2019**, *10*, 1651.
[22] Y. Zhou, X. Guan, H. Zhou, K. Ramadoss, S. Adam, H. Liu, S. Lee, J. Shi, M. Tsuchiya, D. D. Fong, S. Ramanathan, *Nature* **2016**, *534*, 231.
[23] C. Huang, J. Anderson, S. Peana, X. Chen, S. Ramanathan, D. Weinstein, *J. Microelectromech. Syst.* **2021**, *30*, 488.
[24] H.-T. Zhang, T. J. Park, A. N. M. N. Islam, D. S. J. Tran, S. Manna, Q. Wang, S. Mondal, H. Yu, S. Banik, S. Cheng, H. Zhou, S. Gamage, S. Mahapatra, Y. Zhu, Y. Abate, N. Jiang, S. K. R. S. Sankaranarayanan, A. Sengupta, C. Teuscher, S. Ramanathan, *Science* **2022**, *375*, 533.
[25] R. S. Bisht, J. Park, H. Yu, C. Wu, N. Tilak, S. Rangan, T. J. Park, Y. Yuan, S. Das, U. Goteti, H. T. Yi, H. Hijazi, A. Al-Mahboob, J. T. Sadowski, H. Zhou, S. Oh, E. Y. Andrei, M. T. Allen, D. Kuzum, A. Frano, R. C. Dynes, S. Ramanathan, *Nano Lett.* **2023**, *23*, 7166.
[26] F. Zuo, P. Panda, M. Kotiuga, J. Li, M. Kang, C. Mazzoli, H. Zhou, A. Barbour, S. Wilkins, B. Narayanan, M. Cherukara, Z. Zhang, S. Sankaranarayanan, R. Comin, K. M. Rabe, K. Roy, S. Ramanathan, *Nat. Commun.* **2017**, *8*, 240.
[27] D. K. Amarasinghe, H. Yu, F. Rodolakis, H. Zhou, H. Cao, S. Ramanathan, *J. Solid State Chem.* **2022**, *315*, 123512.
[28] L. Si, W. Xiao, J. Kaufmann, J. M. Tomczak, Y. Lu, Z. Zhong, K. Held, *Phys. Rev. Lett.* **2020**, *124*, 166402.
[29] C. Qin, M. Jiang, L. Si, *Phys. Rev. B* **2023**, *108*, 155147.
[30] P. P. Balakrishnan, D. Ferenc Segedin, L. E. Chow, P. Quarterman, S. Muramoto, M. Surendran, R. K. Patel, H. LaBollita, G. A. Pan, Q. Song, Y. Zhang, I. El Baggari, K. Jagadish, Y.-T. Shao, B. H. Goodge, L. F. Kourkoutis, S. Middey, A. S. Botana, J. Ravichandran, A. Ariando, J. A. Mundy, A. J. Grutter, *Nat. Commun.* **2024**, *15*, 7387.
[31] S. Zeng, C. S. Tang, Z. Luo, L. E. Chow, Z. S. Lim, S. Prakash, P. Yang, C. Diao, X. Yu, Z. Xing, R. Ji, X. Yin, C. Li, X. R. Wang, Q. He, M. B. H. Breese, A. Ariando, H. Liu, *Phys. Rev. Lett.* **2024**, *133*, 066503.
[32] M. Gonzalez, A. Ievlev, K. Lee, W. Kim, Y. Yu, J. Fowlie, H. Y. Hwang, *Phys. Rev. Mater.* **2024**, *8*, 084804.
[33] S. Di Cataldo, P. Worm, L. Si, K. Held, *Phys. Rev. B* **2023**, *108*, 174512.
[34] A. Malashevich, S. Ismail-Beigi, *Phys. Rev. B* **2015**, *92*, 144102.
[35] M. Kotiuga, Z. Zhang, J. Li, F. Rodolakis, H. Zhou, R. Sutarto, F. He, Q. Wang, Y. Sun, Y. Wang, N. A. Aghamiri, S. B. Hancock, L. P. Rokhinson, D. P. Landau, Y. Abate, J. W. Freeland, R. Comin, S. Ramanathan, K. M. Rabe, *Proc. Natl. Acad. Sci.* **2019**, *116*, 21992.
[36] H. Chen, M. Dong, Y. Hu, T. Lin, Q. Zhang, E.-J. Guo, L. Gu, J. Wu, Q. Lu, *Nano Lett.* **2022**, *22*, 8983.
[37] M. Hepting, D. Li, C. J. Jia, H. Lu, E. Paris, Y. Tseng, X. Feng, M. Osada, E. Been, Y. Hikita, Y. D. Chuang, Z. Hussain, K. J. Zhou, A. Nag, M. Garcia-Fernandez, M. Rossi, H. Y. Huang, D. J. Huang, Z. X. Shen,

T. Schmitt, H. Y. Hwang, B. Moritz, J. Zaanen, T. P. Devereaux, W. S. Lee, *Nat. Mater.* **2020**, *19*, 381.
[38] P. Wernet, D. Nordlund, U. Bergmann, M. Cavalleri, M. Odelius, H. Ogasawara, L. A. . Naeslund, T. K. Hirsch, L. Ojamaee, P. Glatzel, L. G. M. Pettersson, A. Nilsson, *Science* **2004**, *304*, 995.
[39] M. Yoshida, Y. Mitsutomi, T. Mineo, M. Nagasaka, H. Yuzawa, N. Kosugi, H. Kondoh, *J. Phys. Chem. C* **2015**, *119*, 19279.
[40] J. A. Alonso, M. J. Martínez-Lope, *J. Chem. Soc., Dalton Trans.* **1995**, *17*, 2819.
[41] D. Yi, Y. Wang, O. van 't Erve, L. Xu, H. Yuan, M. J. Veit, P. P. Balakrishnan, Y. Choi, A. T. N'Diaye, P. Shafer, E. Arenholz, H. Grutter, A. Xu, P. Yu, B. T. Jonker, Y. Suzuki, *Nat. Commun.* **2020**, *11*, 902.
[42] N. Takada, T. Uchiyama, Y. Uchimoto, H. Yamagishi, T. Ohta, Y. Orikasa, *Mem. SR Cent. Ritsumeikan Univ.* **2019**, *21*, 3.
[43] M. Al Samarai, A. W. Hahn, A. Beheshti Askari, Y.-T. Cui, K. Yamazoe, J. Miyawaki, Y. Harada, O. Rüdiger, S. DeBeer, *ACS Appl. Mater. Interfaces* **2019**, *11*, 38595.
[44] M. Casas-Cabanas, M. D. Radin, J. Kim, C. P. Grey, A. Van der Ven, M. R. Palacín, *J. Mater. Chem. A* **2018**, *6*, 19256.
[45] D. Li, K. Lee, B. Wang, M. Osada, S. Crossley, H. R. Lee, Y. Cui, Y. Hikita, H. Y. Hwang, *Nature* **2019**, *572*, 624.
[46] S. Asanuma, P. H. Xiang, H. Yamada, H. Sato, I. H. Inoue, H. Akoh, A. Sawa, K. Ueno, H. Shimotani, H. Yuan, M. Kawasaki, Y. Iwasa, *Appl. Phys. Lett.* **2010**, *97*, 14.
[47] L. Gao, H. Wang, F. Meng, H. Peng, X. Lyu, M. Zhu, Y. Wang, C. Lu, J. Liu, T. Lin, A. Ji, Q. Zhang, L. Gu, P. Yu, S. Meng, Z. Cao, N. Lu, *Adv. Mater.* **2023**, *35*, 2300617.
[48] M. Kawai, S. Inoue, M. Mizumaki, N. Kawamura, N. Ichikawa, Y. Shimakawa, *Appl. Phys. Lett.* **2009**, *94*, 082102.
[49] Q. Yang, J. Lee, H. Jeen, H. J. Cho, H. Ohta, *ACS Appl. Electron. Mater.* **2021**, *3*, 3296.
[50] J. Chen, W. Mao, L. Gao, F. Yan, T. Yajima, N. Chen, Z. Chen, H. Dong, B. Ge, P. Zhang, X. Cao, M. Wilde, Y. Jiang, T. Terai, J. Shi, *Adv. Mater.* **2020**, *32*, 1905060.
[51] L. J. Bannenberg, B. Boshuizen, F. A. Ardy Nugroho, H. Schreuders, *ACS Appl. Mater. Interfaces* **2021**, *13*, 52530.
[52] F. Baiutti, G. Christiani, G. Logvenov, *Beilstein J. Nanotechnol.* **2014**, *5*, 596.
[53] J. Daillant, A. Gibaud, *X-ray and Neutron Reflectivity: principles and applications*, Springer, Berlin **2009**.
[54] E. Benckiser, Y. Khaydukov, L. Guasco, K. Fürsich, P. Radhakrishnan, G. Kim, B. Keimer, *Phys. Status Solidi B* **2022**, *259*, 2100253.
[55] A. P. Le Brun, T.-Y. Huang, S. Pullen, A. R. J. Nelson, J. Spedding, S. A. Holt, *J. Appl. Crystallogr.* **2023**, *56*, 18.
[56] L. J. Bannenberg, R. Bresser, P. van der Ende, M. van Exter, W. van Goozen, F. Naastepad, M. A. Thijs, M. N. Verleg, K. de Vroege, R. Waaijer, A. A. van Well, *Rev. Sci. Instrum.* **2023**, *94*, 113901.
[57] A. R. J. Nelson, S. W. Prescott, *J. Appl. Crystallogr.* **2019**, *52*, 193.
[58] M. Bjorck, G. Andersson, *J. Appl. Crystallogr.* **2007**, *40*, 1174.
[59] T. K. Y. Khaydukov, O. Soltwedel, *J. Large-Scale Res. Facil.* **2015**, *1*, A38.
[60] S. Roobol, W. Onderwaater, J. Drnec, R. Felici, J. Frenken, *J. Appl. Crystallogr.* **2015**, *48*, 1324.